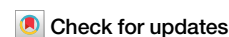


<https://doi.org/10.1038/s43246-025-00787-2>

High-temperature mid-wavelength infrared avalanche photodiode with modified fully-depleted absorption and multiplication region



Liqi Zhu^{1,5}✉, Zihao Wang^{1,2,5}, Jiamu Lin¹✉, Jian Huang¹, Linxuan He³, Xi Wang¹, Songmin Zhou¹, Zhikai Gan¹, Xun Li¹, Qingxin Li¹, Li He¹, Changqing Lin^{1,4}, Chun Lin^{1,2}✉ & Baile Chen^{1,2}

Mid-wavelength infrared (MWIR) avalanche photodiodes (APD) are extensively employed in high-precision detection and thermal imaging in complex context. However, conventional MWIR APD's detection typically requires low-temperature operation to relieve signal-to-noise limitations imposed by narrow bandgap materials. Here, to address this challenge, we present the high-temperature-operating MWIR avalanche photodiodes with a modified fully-depleted absorption, multiplication region (MFDAM) to suppress the high dark current. At 80 K, the proposed APD achieves comparable gain-normalized dark current density (GNDCD) still $<6 \times 10^{-10}$ A/cm² at gain <20 . At 160 K, the GNDCD preserves consistently below 2×10^{-6} A/cm² for gain values less than 189, while the excess noise holds below 1.4 and the noise equivalent power is $<7.2 \times 10^{-16}$ W/Hz^{1/2} of 3.5 μ m. The device is also validated for imaging targets up to 200 km away at a gain of <10 . These results enable the MFDAM APDs to be promising and desirable for future high-temperature-operating MWIR detection applications.

Mid-wavelength infrared detectors are widely employed in a multitude of fields¹, including missile early warning and tracking, night vision imaging^{2,3}, target recognition^{4,5}, environmental monitoring⁶, astronomical observation^{7,8}, scientific research^{9,10}, as well as medical and biological applications^{5,11}. However, the optical absorption caused by carbon dioxide and water vapor in the atmosphere significantly attenuates the system signal¹². Additionally, achieving accurate long-range detection and tracking of weak targets in low-light and complex environments requires devices capable of amplifying signals during the detection process to enhance the signal-to-noise ratio (SNR) at the receiver output. Avalanche photodiodes (APDs), which integrate both the detection and intrinsic gain stages into a single device, greatly improve detection accuracy and resolution, thereby playing a critical role in such weak signal application systems. However, traditional MWIR APDs are typically operated at liquid nitrogen temperatures due to the uncontrollable tunneling current suffered by narrow bandgap devices in response to large multiplication gain^{13–15}, the dark current is still the main limiting issue for current MWIR APDs. Moreover, MWIR APD systems are also appealed to operate at higher temperatures to reduce cost and power consumption,

making them more suitable for demanding environments and paving the way for extending their versatility in the commercial, scientific and civilian applications^{16,17}. But more importantly, the APDs inherently contribute to an increase in shot noise, $\langle i_{\text{shot}}^2 \rangle = 2qM^2(I_{\text{ph}} + I_{\text{d}})F(M)\Delta f$, by generating an excess noise factor, $F(M) = kM + (1-k)(2-1/M)$, where k is the ratio of electron impact ionization coefficient α to hole β , due to the stochastic nature of the impact ionization process^{18,19}. Therefore, the exploitation of the next-generation MWIR APDs must be equipped with both low dark current, high temperature operation (HOT), and low excess noise factor.

The popular InAs and Hg_{1-x}Cd_xTe homogeneous *p-i-n* devices are widely used for MWIR detection and amplification that exhibits a high gain and low excess noise at liquid nitrogen temperature^{20,21}. However, when operating at higher temperatures, the devices reveal poor band-to-band tunneling current for InAs¹³ and high diffusion dark current due to the low *p*-type doping concentration ($<5 \times 10^{16}$ cm⁻³) for HgCdTe^{22,23}.

The Sb-based materials, such as AlInAsSb¹⁹, AlGaAsSb²⁴, AlAsSb²⁵, feature a large spin-orbit splitting energy (Δ_{so}) to bandgap energy ratio,

¹National Key Laboratory of Infrared Detection Technologies, Shanghai Institute of Technical Physics, Chinese Academy of Sciences, Shanghai, China. ²School of Information Science and Technology, ShanghaiTech University, Shanghai, China. ³School of Microelectronics, Shanghai University, Shanghai, China. ⁴University of Chinese Academy of Sciences, Beijing, China. ⁵These authors contributed equally: Liqi Zhu, Zihao Wang. ✉e-mail: zhuliqi@mail.sitp.ac.cn; linjiamu@mail.sitp.ac.cn; chun_lin@mail.sitp.ac.cn

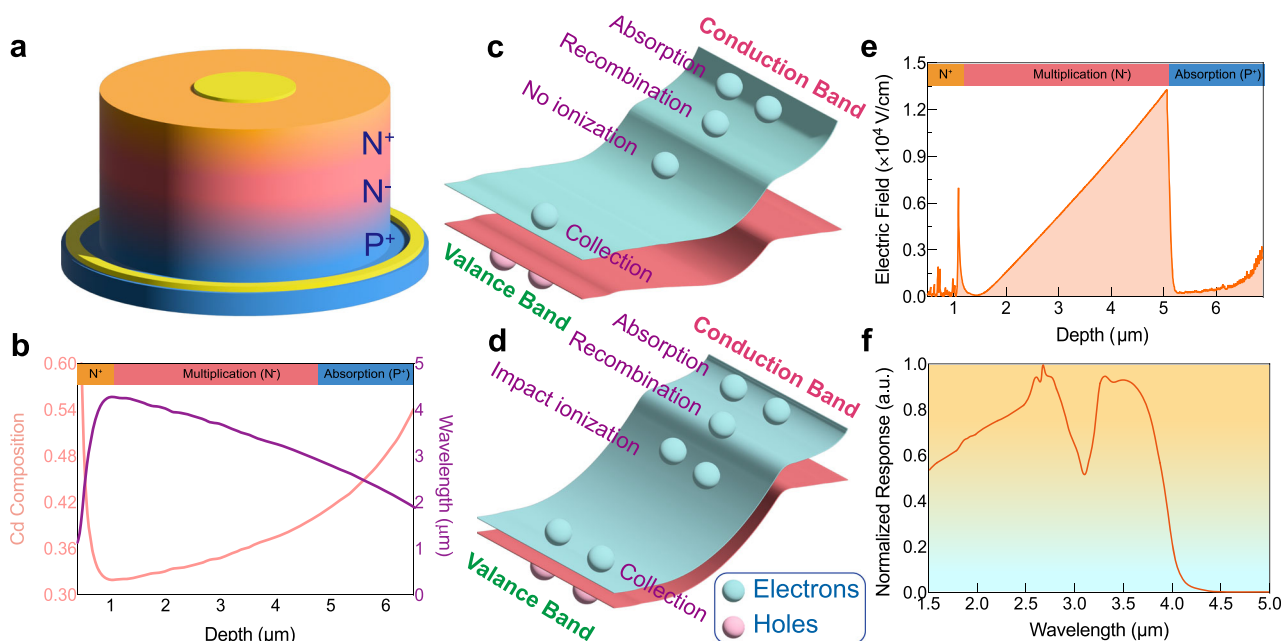


Fig. 1 | Modified fully-depleted absorption, multiplication region HOTA MWIR APD structure. a Schematic diagram of HgCdTe MWIR avalanche photodiodes with fully depleted absorber layer, the material is composed of multiple layers of composition gradients. **b** The distribution of Cd composition and the corresponding wavelength at 80 K for proposed MFDAM APD, whose absorption region is a wide bandgap (refers to high composition) altered. The absorbed photon-generated electrons (two in conduction band) will go through the three processes: recombination occurs after absorption (one electron remains), drift to the multiplication region for impact ionization (two electrons in (d)), relaxation in collection region (one electron in (c) and two in (d)). The absorbed two photon-

generated holes in the valence band will have no impact ionization happens. The blue and pink circles indicate electrons and holes, respectively. **e** Modeled electric field profile of the structure showing that the absorber layer is depleted due to the presence of a built-in electric field. This phenomenon arises from the energy differences between the conduction and valence bands caused by the interaction of materials with different bandgaps. The diffusion of carriers leads to band bending, resulting in a redistribution of carriers near the contact surface, which, in turn, forms a space charge region and generates an electric field at the interface. **f** The normalized spectrum response of the proposed MWIR MFDAM APD device at 80 K.

which can significantly reduce the holes impact ionization coefficients β , representing the most promising candidates for achievable low excess noise factor APDs. They combine the merit of separate absorption, charge, and multiplication (SACM) structure, which maintains a large electric field in a wide bandgap-multiplication region to achieve the high gain, while keeping the electric field in the narrow bandgap-absorption region below the threshold of the tunneling current, to realize a high-performance 1550 nm and 2 μm detection APD devices. The researchers also attempt to extend the Sb-based APD's operating wavelength toward the mid-infrared. However, APDs still suffer from large dark current when operating at wavelengths above 3 μm, and there is no proven way to address it^{26–28}.

In this paper, we present the modified fully-depleted absorption, multiplication (MFDAM) high-temperature-operation HgCdTe MWIR APD structure by employing the bandgap-engineering. The device represents the breakthrough of the dark current density and gain-normalized dark current density (GNDCD) at high gains and high temperature over 160 K. At 160 K, the device exhibits a multiplication gain of 189 with extremely low excess noise $F < 1.4$, a noise equivalent power (NEP) of less than 7.2×10^{-16} W/Hz^{1/2} at 3.5 μm and an excellent GNDCD below 2×10^{-6} A/cm². The imaging results demonstrate that the APD device is capable of capturing signals for remote sensing at distances exceeding 200 km. These findings reveal that the MFDAM APDs are promising for future high-temperature-operating MWIR detection and likely the photon-starved applications.

Results

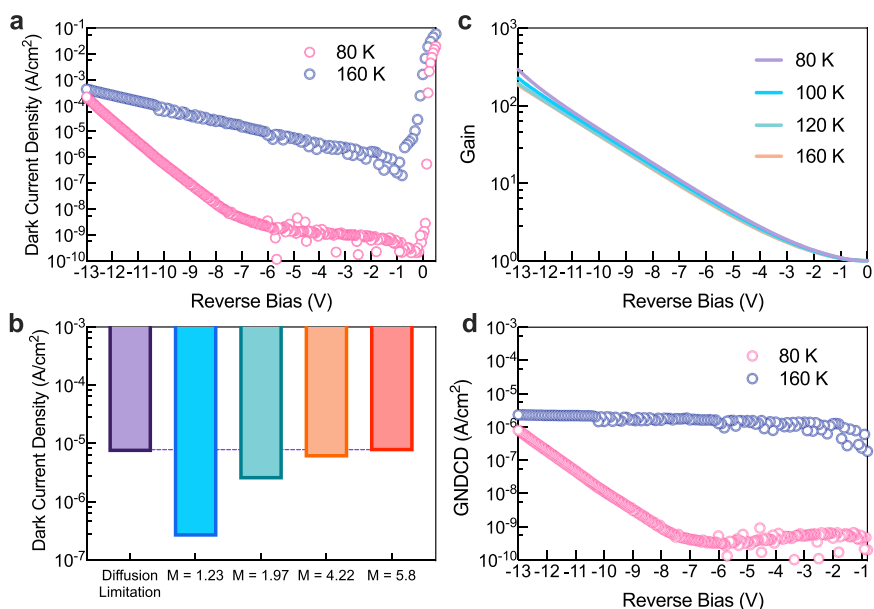
Device and design

The specific structural details of the heterostructure MFDAM APD is illustrated in Fig. 1a. Processes of the material growth and device fabrication are provided in the Sec. “Methods”. In contrast to the SACM structure

commonly employed in III-V group materials, which features a narrow bandgap in the absorption region and a wide bandgap in the multiplication region. The MFDAM device is accomplished by creatively incorporating composition-graded multilayer wide-bandgap Hg_{1-x}Cd_xTe materials within the absorption region along with composition-graded narrow-bandgap Hg_{1-x}Cd_xTe materials within the multiplication region, the distribution of Cd composition and cutoff wavelength relative to the device depth is shown in Fig. 1b. Here, the energy bands in which they meet are smooth and continuous to ensure that mid-wavelength photons move into the multiplication region to acquire energy for impact ionization events. Compared with the standard device, this device is unique in that the grading is completely covering the whole structure, which makes sure that the benefits of the different compositions are well appreciated in the different layers. On the one hand, the introduced wide-bandgap gradient material in the absorption region is to generate a built-in quasi-electric field, which is different from the SACM structure but attempts to deplete the layer over a composition grading and serves to mitigate the influence of diffusion current. Additionally, the composition-gradient can effectively drive carriers away from surface states, while the larger bandgap of the short-wavelength material reduces the non-radiative recombination of carriers in the absorption region. Together, these two effects contribute to the overall suppression of the device's dark current. The multiplication region, composed of narrow-bandgap materials with a graded composition, can provide a high electron impact ionization gain and low excess noise while suppressing tunneling current by carefully designing the thickness. In Hg_{1-x}Cd_xTe material systems, the reduction of Cd composition makes the bandgap energy notably smaller than $\Delta\epsilon_0$ at longer wavelengths, resulting in the impact ionization rate of holes being greatly reduced¹⁵. Thus, exponential gain and low excess noise are enabled. Besides, only graded composition can further minimize the influence of tunneling current for

Fig. 2 | Dark Current and multiplication gain measurements.

a Measured dark current density versus voltage curves of a $100\ \mu\text{m} \times 100\ \mu\text{m}$ device at 80 K and 160 K temperature. **b** Comparison of dark current density at different gains with the theoretical limit of electron diffusion current at 160 K. It is always less than the diffusion limit with a gain $M < 5.8$. **c** The measured multiplication gain along with the reverse bias at the temperature 80 K–160 K for $100\ \mu\text{m} \times 100\ \mu\text{m}$ device. The maximum gain is $M = 189$ at 160 K. **d** The calculated GNDCD at 80 K and 160 K, the dark current density and gain are from (a) and (c).



narrow-bandgap materials. Finally, a little thickness of wide-bandgap materials in the device surface is used to effectively reduce the surface leakage current²⁹. Fig. 1c and d show the energy band diagrams for the device at zero bias and large reverse bias. It can be seen that the electric field is mainly located at the multiplication region as the calculated electric field profile in Fig. 1e, while the absorption region is fully depleted by the built-in electric field. As a result, the MFDAM APD device demonstrates that the mid-wavelength infrared response can be up to $4.2\ \mu\text{m}$ under the 80 K temperature due to the combined efforts of all compositions, as shown in Fig. 1f.

Dark current density and gain

Figure 2(a) displays the measured dark current density of the $100\ \mu\text{m} \times 100\ \mu\text{m}$ APD device under 80 K and 160 K. It can be noted that the dark current density is lower than $1 \times 10^{-9}\ \text{A}/\text{cm}^2$ at bias $< -6\ \text{V}$ of 80 K due to the presence of wide-bandgap composition gradient and significantly improved over previous conventional homojunction devices^{15,22}. Besides, the band-to-band tunneling current is also effectively weakened, which is obviously observed at the high temperature of 160 K. In order to evaluate the ability of MFDAM MWIR APD device to operate at elevated temperatures, the dark current density of 160 K is quantified to provide a distinct comparison to the theoretical n/p diffusion-limited benchmark^{30,31}. The results are shown in Fig. 2b, it can be clearly identified that the dark current density is nearly an order of magnitude lower than the diffusion limitation at unit gain bias and corresponding to it at large gain $M = 5.8$. The temperature-dependent dark current density is also provided in Supplementary Fig. S3, the results also exhibit excellent performance even if the operating temperature continues to improve. Besides, the activation energy, which is about half the bandgap, indicates that the proposed APD device is dominated by the generation-recombination (G-R) current at the high temperature. Improvements in minority carrier lifetime to reduce the G-R current will be a benefit to the device's future operation at higher temperatures.

The multiplication gain is characterized by phase-sensitive technology in “Methods”, the measured gain along with the reverse bias at the temperature 80 K–160 K for $100\ \mu\text{m} \times 100\ \mu\text{m}$ device is shown in Fig. 2c. It is discovered that the overall gain decreases as temperature increases, which is attributed to the decrease in the impact ionization coefficient due to the increase in the bandgap as well as the electrons effective mass. The exponential gain is responsible for the pure electrons impact ionization, as explained in previous reports¹⁵. A high gain of 189 at $-13\ \text{V}$ bias is also

achieved under the 160 K high temperature. With a bias greater than $-13\ \text{V}$, significantly higher gains can be expected, reaching to 1000 at low temperatures of 80 K.

The general evaluation of the APDs is usually examined by the gain-normalized dark current density (GNDCD), which is determined by the measured dark current density and multiplication gain. Fig. 2d shows the GNDCD versus the reverse bias at 80 K and 160 K. The MFDAM APD performed the lowest GNDCD of $4 \times 10^{-10}\ \text{A}/\text{cm}^2$ under $-7\ \text{V}$ bias with a gain of 11 at 80 K. Moreover, at high temperatures 160 K, the recorded GNDCD is consistently less than $2 \times 10^{-6}\ \text{A}/\text{cm}^2$, even at large gains of 189. Therefore, it can be inferred from the experimental results that the wide-bandgap composition gradient successfully addresses the limitations of the dark current for high-temperature operation, while the narrow-bandgap gradient also enables a large gain at high temperatures.

Excess noise

The measured excess noise factor (F) of the MFDAM structure is revealed as a function of gain, as shown in Fig. 3a. The design exhibits extremely low excess noise below the local field model limitation of 2^{32} , which can be explained and developed by the latest non-local field theory³³. The excess noise factor is of 1.39 at the gain of 160 for 160 K operating. In the lower gain range, the excess noise increases as the fact that the average impact ionization length remains greater than the dead space, and the increase of uncertainty in the impact ionization process^{15,33}. The low excess noise Sb-based APDs^{24,26,34,35} and previous HgCdTe APD²⁹ are employed to compare with the MFDAM structure, results are concluded in Fig. 3(b). The MFDAM APD is proved that can carry out higher gain at elevated temperature as well as the lower excess noise. This is mainly due to the fact that narrow-bandgap gradient can effectively hold down the tunneling current to ensure that the device can be operated at a higher bias voltage.

Quantum efficiency

Spectral response measurements were used to determine the external quantum efficiency (EQE) of the extended MFDAM APDs. Fig. 4a displays the spectral EQE and responsivity obtained of an MFDAM APD under $-0.2\ \text{V}$ voltages at 80 K and 160 K temperatures. The device exhibits a cutoff wavelength of $\sim 4.1\ \mu\text{m}$ at 160 K, and the EQE at $3\ \mu\text{m}$ is about 40%, the maximum EQE is of 45% at $2.67\ \mu\text{m}$ wavelength. It should be noted that the lateral collection length that comes from the neighboring pixel is also considered as depicted in “Methods”. The comparatively low quantum efficiency can be attributed to the reduced thickness of the absorbing

Fig. 3 | Excess noise measurements. **a** The excess noise versus multiplication gain of the proposed $100\ \mu\text{m} \times 100\ \mu\text{m}$ APD device at 80 K, 160 K, and 200 K. **b** The comparison of different low-excess-noise APDs at different wavelengths and working temperatures with this work. The color of the solid circles represents the working temperature shown in the temperature bar, and the label around the circles indicates the cutoff wavelength.

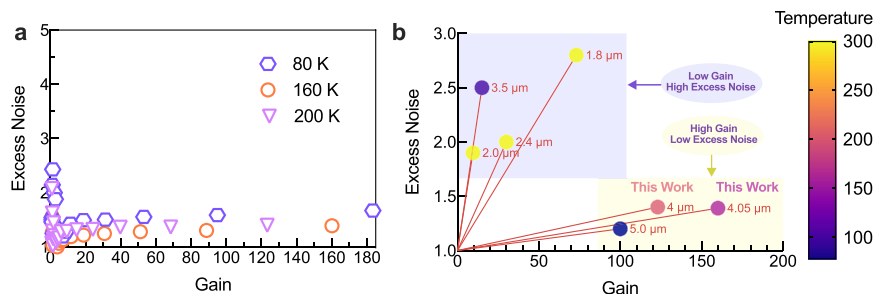


Fig. 4 | Quantum efficiency and noise equivalent power measurements. **a** Measured unity-gain external quantum efficiency and responsivity of a $100\ \mu\text{m} \times 100\ \mu\text{m}$ APD device at 80 K and 160 K. **b** The noise equivalent power versus wavelength under 292 gain for 80 K and 189 gain for 160 K. The noise is based on the measured dark current under the $-13\ \text{V}$ bias.

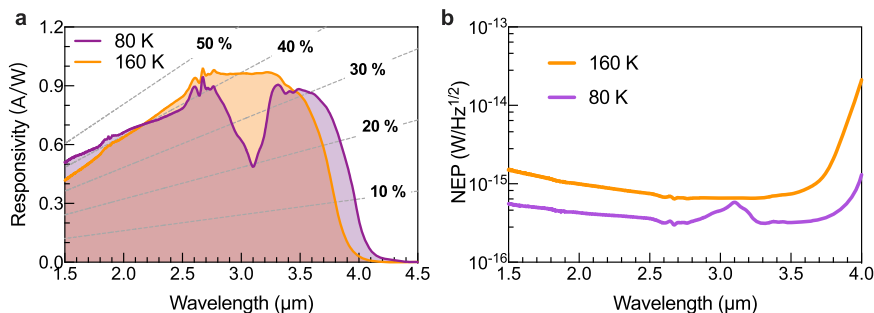


Fig. 4b. For 160 K and 189 gain, the NEP is below $< 7.2 \times 10^{-16}\ \text{W}/\sqrt{\text{Hz}}$ of $3.5\ \mu\text{m}$ wavelength, the value is slightly increase for wavelength low than $3.5\ \mu\text{m}$ as the responsivity decrease, but the obtained results are still less than the $2 \times 10^{-15}\ \text{W}/\sqrt{\text{Hz}}$. These figures all point to the fact that the MFDAM APD device is an excellent performance at high temperature 160 K.

Weak signal imaging

Next, to extend the applications and prove the performance more balanced, a small arrays that produced with MFDAM MWIR APDs are used to image targets in complex contexts at remote distances, since the high performance APD device can achieve improved signal-noise-ratio (SNR) due to the internal multiplication gain compared with the normal MWIR device. In this work, we demonstrate the devices for imaging at gains below 10, where they have a low dark current density and NEP as well as high uniformity. Figure 5 presents the imaging results at varying distances while a civil aviation aircraft passes overhead. It can be observed that the target is located at 80 km, where the SNR is 93 dB, a clear pattern is obtained including the tail flame. As the distance increases, the signal strength diminishes, leading to a greater prominence of noise contributions from the sensor and the surrounding environment. However, the advanced design of our MWIR APD devices makes it possible to increase the signal value without significantly introducing heavy dark currents and noise. Thus, the tail flame can be visualized at target distances greater than 200 km, even if the environment is severely attenuating the signal and the field of view is reducing.

Discussion

Table 1 presents a comparative analysis of our work alongside other emerging III-V MWIR SACM APDs, including an AlInAsSb-AlInAsSb^{26,36,37}, InAs/GaSb-AlAsSb²⁷, InAs-AlAsSb²⁸, InGaAs/GaAsSb-AlGaAsSb³⁴, respectively, as well as the traditional InAs³⁸, HgCdTe³⁰ APDs. It is evident that our device stands out for its performance in all metrics. Especially, the longer cutoff wavelength of $4.1\ \mu\text{m}$ in our structure versus the AlInAsSb APD ($< 3.5\ \mu\text{m}$) means that more infrared information can be obtained at comparable temperatures to satisfy the extensive applications domains. The lower gain normalized dark current density ensures that the APD operates at high gains without cooling down the temperature. There is

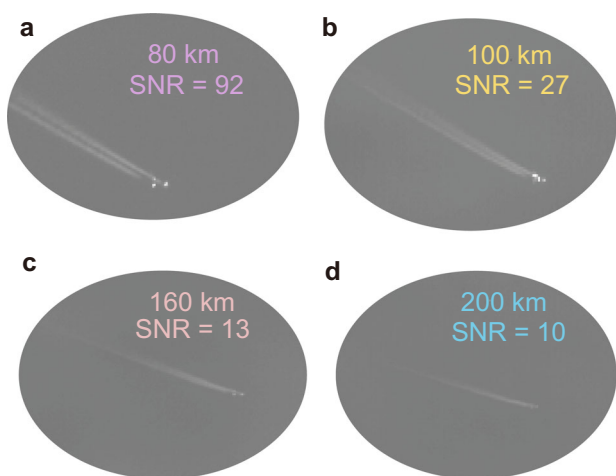


Fig. 5 | Imaging of targets at long distance. The proposed MFDAM APD devices are utilized for imaging weak targets at varying long distances of (a). 80 km, (b). 100 km, (c). 160 km and (d) 200 km.

composition, as illustrated in Fig. 1b, Incident photons do not travel a sufficient distance to be well absorbed, particularly in the mid-infrared region where the photons diffusion length is relatively long. Besides, in extending the short-wavelength range, the recombination results in the absorbed carriers being unable to effectively contribute to the photocurrent. Future improvements in quantum efficiency may focus on several approaches, including the incorporation of anti-reflection (AR) coating²⁶ or photon-trapping³⁵ as potential solutions. The fundamental objective is to enhance the thickness of the absorbing composition while minimizing any adverse impact on the dark current.

The noise equivalent power (NEP) is a widely used figure of merit for APD-based receivers, representing the minimum detectable light signal. Consequently, a lower NEP indicates superior performance. In this MFDAM APD device, the NEP is calculated by the measured dark current, gain as well as the responsivity, the results under $-13\ \text{V}$ are all shown in

Table 1 | Summary of the Reported MWIR APDs for HOT

Reference	Absorption Layer Material	Multiplication Layer Material	Operating temperature (K)	Maximum gain	GNDCD (mA/cm ²)	Cutoff wavelength (μm)
This work	Wide-bandgapgradient Hg_{1-x}Cd_xTe	Narrow-bandgapgradient Hg_{1-x}Cd_xTe	160	~189	< 0.002	~4.1
26	Al _{0.05} InAsSb	Al _{0.7} InAsSb	100	~850	0.05	~3.5
36	Al _{0.15} InAsSb	Al _{0.7} InAsSb	100	~380	6	~2.9
37	Al _{0.3} InAsSb	Al _{0.7} InAsSb	180	~200	0.006 @ M = 10	~2.0
27	InAs/GaSb	AlAs _{0.06} Sb _{0.94}	150	~15.9	0.38	~3.28
28	InAs	Al _{0.13} As _{0.87} Sb	300	~13.1	47.7	~3.5
38	InAs	InAs	140	~105	0.7	~3.2
34	InGaAs/GaAsSb	AlGaAsSb	300	~180	5.5 @ M=10	~2.4
30	HgCd _{0.33} Te	HgCd _{0.33} Te	160	~648	0.039	~4.06
39	HgCd _{0.4} Te	HgCd _{0.4} Te	180	~45	0.004	~3

Boldface denotes the results of this work.

also an order of magnitude advantage over HgCd_{0.33}Te (0.039 mA/cm²) in the same condition. In general, this device departs from the traditional SACM structure, which employs the short-wavelength material in the multiplication region to suppress the tunneling current. Additionally, the MFDAM APD, with a fully depleted short-wavelength absorption region, can ensure that the device's dark current is primarily governed by the generation-recombination process. Besides, the short-wavelength region exhibits a lower intrinsic carrier concentration n_i and a longer carrier lifetime τ_{SR} , which can diminish the generation-recombination current ($J_{gr} \propto n_i \times 1/\tau_{SR}$, vs. $J_{diff} \propto n_i^2 \times (1/\tau_A + 1/\tau_{SR})$) that is significantly superior to the diffusion current and thus prove transformative in achieving enhanced performance for mid-wavelength infrared devices.

Conclusion

In conclusion, we have demonstrated MFDAM APDs with composition-graded HgCdTe materials for a large gain, low excess noise, low GNDCD, >4 μm cutoff at elevated temperature of 160 K, which was previously deemed not possible for MWIR APDs. The whole performances are improved by optimizing the distribution of composition and multiplication region parameters. At 160 K, our device exhibits the GNDCD preserves consistently below 2×10^{-6} A/cm² for gain values less than 189, while the excess noise holds below 1.4 and the noise equivalent power is $<7.2 \times 10^{-16}$ W/Hz^{1/2} of 3.5 μm. This device achieves GNDCD and excess noise better than previously best MWIR APDs, and these results are promising for high-temperature-operation MWIR APD detection applications, in the meantime, defending the absolute dominance of HgCdTe-based APDs. For the future, improving quantum efficiency and optimizing minority carrier lifetimes are at the heart of the efforts.

Methods

Material growth and device fabrication

The n-type low doping concentration ($<5 \times 10^{14}$ cm⁻³) Hg_{1-x}Cd_xTe thin film was grown on an infrared transparent (111) CdZnTe substrate using vertically liquid-phase epitaxy (LPE) technology. As the Cd composition difference between the CdZnTe and Hg_{1-x}Cd_xTe interface on the back of the material, the high-temperature and long-time inter-diffusion annealing was employed to deliver the grading to cover the whole structure. The CdTe/Hg_{1-x}Cd_xTe interface on the surface of the material was also treated, as shown in Fig. 1, the composition distribution of the final material. The XRD patterns are provided in the Supplementary Fig. S2 to analyse the material quality. The p⁺ absorption layer of the device was doped by Hg-vacancy with $1\sim2 \times 10^{16}$ cm⁻³. The n⁺ region was obtained by B⁺ ions implantation. Through a certain period of rapid annealing treatment, the n⁻ multiplication region of low doping ($<5 \times 10^{14}$ cm⁻³) could be formed. The device was then covered by a ZnS/CdTe double passivation layer to suppress the surface leakage current. The mesa is corroded by the 0.3% HBr. Finally, Cr/

Au (50/150 nm) was deposited for n-contacts and p-contacts using an e-beam evaporator. The final device is pictured by the SEM in Supplementary Fig. S1.

Current-voltage characterization

Current-voltage (I-V) characteristics were measured with a Keithley 6430 source meter under blackout condition at different temperature for various device size, as shown in Supplementary Fig. S3.

Multiplication gain

The net photocurrent was measured with a blackbody source (T = 700 °C), a Fast Fourier Transform (FFT) analyzer, and a low-noise preamplifier. A mechanical chopper modulated the blackbody light at 130 Hz to remove DC dark current, and a Keithley 2901 source meter unit was used to apply the bias. The multiplication gain M(V) was calculated as the ratio of the net photocurrent (I_{net}) at bias V to that measured at the unity gain point of -0.5 V. It was noted that the gain calculation has considered the slight increase of injected photocurrent with reverse bias due to the widening of the depletion width given the long diffusion length of HgCdTe materials.

$$M(V) = \frac{I_{net}(V)}{I_{net}(-0.5)} \quad (1)$$

Excess noise

The proposed MFDAM MWIR APD was biased at different temperature with a Keithley 2400 source meter. A 1550 nm continuous-wave laser was used to illuminate the APDs. The alternating current component of the output current was measured with an Agilent 8970 B noise figure analyser with a 50 Ω load impedance through a standard radio frequency bias tee. Careful system calibration was carried out via a calibrated Agilent 346A noise source to remove background noise. Devices were measured over a 4 MHz bandwidth centered at 20 MHz. Supplementary Fig. S4 describes the linearity of photocurrent versus normalized noise power for different light intensities at unit gain. The slope A_{slope} of the linear fit is used to calculate the excess noise factor for different gains at constant optical power.

$$S_{unit} = 2qB \cdot I_{unit} = A_{slope} \cdot I_{unit} \quad (2)$$

$$S_M = 2qB \cdot I_{unit} M^2 F = A_{slope} \cdot I_{unit} \cdot M^2 F \quad (3)$$

Quantum efficiency

The response spectrum and quantum efficiency of the backside-illuminated device were measured by a Fourier transform infrared spectrometer (FTIR) and calibrated by a 700 °C blackbody source. The calibration of the

responsivity includes the effect of the lateral collection length, which correlated with the crosstalk signal of neighboring pixels in the array and resulted in the optical collection radius (L_c) being larger than the actual device radius (L_r). Here, the lateral optical length L_c could be determined by measuring the photocurrent I_{ph} of the diodes with different device radius L_r using the following equation, where the I_{ph-1D} is the photocurrent collected by a diode with no lateral collection. The fitting result based on the different device radius is drawn in Supplementary Fig. S5.

$$I_{ph} = I_{ph-1D} \cdot \left(1 + \frac{L_c}{L_r}\right)^2 \quad (4)$$

Numerical simulation

The theoretical model was established with a commercial software package Silvaco TCAD. The device modeling was developed on the basis of the distribution of composition, which was carried out by the secondary ion mass spectroscopy (SIMS). The energy band structure and electric-field intensity profile were all obtained.

Data availability

The data that support the plots within the paper and other findings of this study are available from the corresponding author upon reasonable request.

Received: 31 December 2024; Accepted: 20 March 2025;

Published online: 12 April 2025

References

- Soref, R. Mid-infrared photonics in silicon and germanium. *Nat. Photonics* **4**, 495–497 (2010).
- Mu, G. et al. Visible to mid-wave infrared pbs/hgte colloidal quantum dot imagers. *Nat. Photonics* 1–8 (2024).
- Zhang, X. & Zhang, Z. W. Fabrication and performance of a nlm2o4/lanio3 composite film detector with multi electrodes for night vision imaging application. *Sens. Actuators A: Phys.* **326**, 112713 (2021).
- Fang, J., Huang, K., Wu, E., Yan, M. & Zeng, H. Mid-infrared single-photon 3d imaging. *Light.: Sci. Appl.* **12**, 144 (2023).
- Shi, L. et al. Mid-infrared metabolic imaging with vibrational probes. *Nat. Methods* **17**, 844–851 (2020).
- Kaufman, Y. J. & Remer, L. A. Detection of forests using mid-ir reflectance: An application for aerosol studies. *IEEE Trans. Geosci. Remote Sens.* **32**, 672–683 (1994).
- Pope, A. et al. Mid-infrared spectral diagnosis of submillimeter galaxies. *Astrophys. J.* **675**, 1171 (2008).
- Wright, G. S. et al. The mid-infrared instrument for JWST and its in-flight performance. *Publ. Astron. Soc. Pac.* **135**, 048003 (2023).
- Schliesser, A., Picqué, N. & Hänsch, T. W. Mid-infrared frequency combs. *Nat. Photonics* **6**, 440–449 (2012).
- Dam, J. S., Tidemand-Lichtenberg, P. & Pedersen, C. Room-temperature mid-infrared single-photon spectral imaging. *Nat. Photonics* **6**, 788–793 (2012).
- Fernandez, D. C., Bhargava, R., Hewitt, S. M. & Levin, I. W. Infrared spectroscopic imaging for histopathologic recognition. *Nat. Biotechnol.* **23**, 469–474 (2005).
- Galli, I. et al. Molecular gas sensing below parts per trillion: Radiocarbon-dioxide optical detection. *Phys. Rev. Lett.* **107**, 270802 (2011).
- White, B. S. et al. High-gain inas planar avalanche photodiodes. *J. Lightw. Technol.* **34**, 2639–2644 (2016).
- Sun, W. et al. High-gain inas avalanche photodiodes. *IEEE J. Quantum Electron.* **49**, 154–161 (2012).
- Zhu, L. et al. Gain and excess noise in hgcdte e-avalanche photodiodes at various temperatures and wavelengths. *IEEE Trans. Electron Devices* **70**, 2384–2388 (2023).
- Klipstein, P. C. et al. Hot mwir technology at scd. In *Infrared Technology and Applications XLVIII*, vol. 12107, 176–184 (SPIE, 2022).
- Rogalski, A., Kopytko, M., Hu, W. & Martyniuk, P. Infrared hot photodetectors: Status and outlook. *Sensors* **23**, 7564 (2023).
- Dadey, A. A., Jones, A. H., March, S. D., Bank, S. R. & Campbell, J. C. Near-unity excess noise factor of staircase avalanche photodiodes. *Optica* **10**, 1353–1357 (2023).
- March, S. D., Jones, A. H., Campbell, J. C. & Bank, S. R. Multistep staircase avalanche photodiodes with extremely low noise and deterministic amplification. *Nat. Photonics* **15**, 468–474 (2021).
- Sun, X. Review of photodetectors for space lidars. *Sensors* **24**, 6620 (2024).
- Anderson, P. D. et al. Recent advancements in hgcdte apds for space applications. *J. Electron. Mater.* **51**, 6803–6814 (2022).
- Zhu, L. et al. Temperature-dependent characteristics of hgcdte mid-wave infrared e-avalanche photodiode. *IEEE J. Sel. Top. Quantum Electron.* **28**, 1–9 (2021).
- Schaaake, H. et al. High-operating-temperature MWIR detector diodes. *J. Electron. Mater.* **37**, 1401–1405 (2008).
- Lee, S. et al. High gain, low noise 1550 nm GaAsSb/alGaAsSb avalanche photodiodes. *Optica* **10**, 147–154 (2023).
- Yi, X. et al. Extremely low excess noise and high sensitivity alas0.56sb0.44 avalanche photodiodes. *Nat. Photonics* **13**, 683–686 (2019).
- Dadey, A. A. et al. High-gain low-excess-noise mwir detection with a 3.5- μ m cutoff alinassb-based separate absorption, charge, and multiplication avalanche photodiode. *APL Photon.* **8**, 036101 (2023).
- Yan, S., Huang, J., Zhang, Y. & Ma, W. Mid wavelength type ii inas/gasb superlattice avalanche photodiode with alassb multiplication layer. *IEEE Electron Device Lett.* **42**, 1634–1637 (2021).
- Huang, J. et al. High-performance mid-wavelength inas avalanche photodiode using alas 0.13 sb 0.87 as the multiplication layer. *Photonics Res.* **8**, 755–759 (2020).
- Zhu, L. et al. Low dark current hgcdte long wavelength infrared photodiodes with bandgap gradient multi-layer heterojunction. *IEEE Electron Device Lett.* **45**, 797–800 (2024).
- Reine, M. et al. Hgcdte mwir back-illuminated electron-initiated avalanche photodiode arrays. *J. Electron. Mater.* **36**, 1059–1067 (2007).
- Gravrand, O. et al. Study of lwir and vlwir focal plane array developments: Comparison between p-on-n and different n-on-p technologies on lpe hgcdte. *J. Electron. Mater.* **38**, 1733–1740 (2009).
- McIntyre, R. Multiplication noise in uniform avalanche diodes. *IEEE Trans. Electron Devices* **1**, 164–168 (1966).
- Rothman, J., Mollard, L., Goût, S., Bonnefond, L. & Wlassow, J. History-dependent impact ionization theory applied to hgcdte e-apds. *J. Electron. Mater.* **40**, 1757–1768 (2011).
- Jung, H. et al. Low excess noise, high quantum efficiency avalanche photodiodes for beyond 2 μ m wavelength detection. *Commun. Mater.* **5**, 219 (2024).
- Chen, D. et al. Photon-trapping-enhanced avalanche photodiodes for mid-infrared applications. *Nat. Photonics* **17**, 594–600 (2023).
- Jones, A. H. et al. Alinassb separate absorption, charge, and multiplication avalanche photodiodes for mid-infrared detection. *IEEE J. Quantum Electron.* **58**, 1–6 (2022).
- Jones, A. H., March, S. D., Bank, S. R. & Campbell, J. C. Low-noise high-temperature alinassb/gasb avalanche photodiodes for 2- μ m applications. *Nat. Photonics* **14**, 559–563 (2020).
- Blain, T. et al. Low noise equivalent power inas avalanche photodiodes for infrared few-photon detection. *IEEE Trans. Electron. Devices* **71**, 3039–3044 (2024).
- Foubert, K. et al. Development of hgcdte single-element apds based detectors for low flux short wave infrared applications. In *Optical Components and Materials X*, vol. 8621, 78–99 (SPIE, 2013).

Acknowledgements

This work was supported in part by the National Key Research and Development Program of China - Civil Space Technology Advance Research Project under Grant D010202, in part by the China Postdoctoral Science Foundation under Grant 2024T170967 and 2024M763411.

Author contributions

Liqi Zhu conceived the design, supervised the project, and wrote the paper. Zihao Wang and Jiamu Lin contributed to device simulation, experiment and analysis. Jian Huang and Linxuan He contributed to layout synthesis and data analysis. Xi Wang contributed to process integration and data analysis. Songmin Zhou, Zhikai Gan, Xun Li, and Qingxin Li contributed to process integration and device fabrication. Changqin Lin contributed to the image capture. Li He, Chun Lin, and Baile Chen oversaw the project.

Competing interests

The authors declare no competing interests.

Additional information

Supplementary information The online version contains supplementary material available at <https://doi.org/10.1038/s43246-025-00787-2>.

Correspondence and requests for materials should be addressed to Liqi Zhu, Jiamu Lin or Chun Lin.

Peer review information *Communications Materials* thanks Seunghyun Lee and the other, anonymous, reviewer(s) for their contribution to the peer review of this work. Primary Handling Editors: John Plummer.

Reprints and permissions information is available at <http://www.nature.com/reprints>

Publisher's note Springer Nature remains neutral with regard to jurisdictional claims in published maps and institutional affiliations.

Open Access This article is licensed under a Creative Commons Attribution 4.0 International License, which permits use, sharing, adaptation, distribution and reproduction in any medium or format, as long as you give appropriate credit to the original author(s) and the source, provide a link to the Creative Commons licence, and indicate if changes were made. The images or other third party material in this article are included in the article's Creative Commons licence, unless indicated otherwise in a credit line to the material. If material is not included in the article's Creative Commons licence and your intended use is not permitted by statutory regulation or exceeds the permitted use, you will need to obtain permission directly from the copyright holder. To view a copy of this licence, visit <http://creativecommons.org/licenses/by/4.0/>.

© The Author(s) 2025